

Infrared Signatures of Dusty Tori Formed by MHD-Driven Outflows

Ruiyu Pan¹ and Arkaprabha Sarangi^{2,3}

¹ Niels Bohr Institute, University of Copenhagen, Lyngbyvej 2, 2100 Copenhagen Ø, Denmark

² Indian Institute of Astrophysics, 100 Feet Road, Koramangala, Bengaluru, Karnataka 560034, India

³ DARK, Niels Bohr Institute, University of Copenhagen, Jagtvej 155A, 2200 Copenhagen, Denmark

ABSTRACT

We investigate the radial structure of active galactic nuclei (AGN) dusty tori by forward-modeling mid-infrared (MIR) spectra observed with JWST/MIRI-MRS for a sample of 25 AGN. We develop a physically motivated three dimensional radiative transfer framework to test various magnetohydrodynamic (MHD) wind scenarios characterized by radial density laws of the form $n(r) \propto r^{-p}$ for $p \in \{0.5, 1.0, 1.5, 2.0\}$. Our Bayesian analysis reveals a pronounced structural dichotomy rather than a single universal density law: a majority (14/25) of the sources favor the flattest profile ($p = 0.5$), while a significant minority (8/25) statistically prefers the steepest, most compact distribution ($p = 2.0$). We also identify a systematic redward shift in the silicate emission peak, consistent with the presence of micron-sized, processed grains in the inner regions of the wind. Critically, we find that the inferred AGN fractional contribution, f_{AGN} , is highly sensitive to the assumed radial index, exhibiting up to a four-fold systematic shift between $p = 0.5$ and $p = 2.0$. This p -degeneracy highlights that static structural assumptions can significantly bias AGN power estimates. The identified structural diversity suggests that MHD-driven winds may exist in multiple dynamical states, though the precise physical drivers governing these configurations remain to be uniquely determined. These results underscore the limitations of single-profile models and emphasize the need for high-resolution spatial constraints to break these fundamental degeneracies.

Key words. galaxies: active – dust, extinction – radiative transfer – methods: numerical – infrared: galaxies

1. Introduction

Interstellar dust plays a crucial role in galaxy evolution by regulating the exchange of energy and matter and reprocessing stellar radiation into the infrared (Draine 2003; Zubko et al. 2004; Hauser & Dwek 2001). Despite its importance, a fundamental tension persists between the observed vast quantities of dust and the limited production capacity of known stellar sources, a mismatch known as the ‘dust budget crisis’ (Dwek & Cherchneff 2011; Jones & Nuth 2011). This crisis is particularly acute in extreme environments like AGN, where dust not only survives intense radiation and strong outflows but is also central to the AGN unification model. In this framework, an optically thick dusty structure, often called a dusty torus, is responsible for the observational dichotomy between type 1 and type 2 AGNs (Antonucci & Miller 1985; Pier & Krolik 1992).

The classical view of a smooth, monolithic dusty torus in AGNs has been challenged by high-resolution interferometric observations, which instead reveal a clumpy, dynamic, and non-axisymmetric structure (Jaffe et al. 2004; Tristram et al. 2007). The survival and replenishment of these dust clumps in close proximity to the central engine deepen the puzzle of the dust budget. This has motivated sophisticated models that incorporate turbulence, radiation pressure, and magnetic fields to explain the structure and kinematics of the torus (Wada et al. 2009; Elvis et al. 2002). Critically, these findings raise the possibility of in-situ dust formation within the AGN environment itself, moving beyond a sole reliance on stellar ejecta.

The dust budget crisis is at its most extreme in the early universe. For instance, the quasar SDSS J1148+5251, seen when the universe was very young ($z = 6.4$), contains a staggering dust mass ($M_{\text{dust}} \sim 10^8 M_{\odot}$), which is about 100 times more than all the stars in that galaxy could possibly have produced (Valiante

et al. 2011). The light from these ancient galaxies shows strong signs of silicate dust, similar to local AGNs, but suggests a distinct chemical evolution compared to typical star-forming galaxies at lower redshifts (Galliano et al. 2018; Imanishi et al. 2023). This suggests that most of this early dust was not made in stars at all, but formed rapidly in powerful outflows driven by magnetic fields, an idea that could fundamentally alter our understanding of how the first galaxies grew (Everett 2005; Gall et al. 2011).

In nearby systems such as NGC 1068, observations provide detailed images of AGN dust structures. Strong $9.7 \mu\text{m}$ silicate absorption and polarized broad-line emission indicate a geometrically and optically thick dusty torus (Antonucci 1993; Tristram et al. 2007). ALMA observations reveal a ring-shaped magnetic field of ~ 10 mG driving molecular outflows at velocities up to $\sim 500 \text{ km s}^{-1}$, consistent with magnetocentrifugal wind models (Lopez-Rodriguez et al. 2020; Blandford & Payne 1982a). Similar high-velocity molecular outflows are seen in high- z quasars like Mrk 231, likely driven by both radiation pressure and MHD mechanisms (Veilleux et al. 2020; Wada 2012). These outflows are often modeled with the dust density law $n(r) \propto r^{-1}$ and $v(r) \propto r^{-0.5}$, in agreement with X-ray and IR observational constraints (Behar et al. 2009; Tristram et al. 2007; Sarangi et al. 2019). More generally, the radial distribution of dusty gas in disk-wind/torus models is uncertain and is frequently parameterized as a power law, $n(r) \propto r^{-p}$ (Narayan & Yi 1994; Narayan et al. 2000; Nenkova et al. 2008; Lopez-Rodriguez et al. 2015; Höning & Kishimoto 2010; García-González et al. 2017). Motivated by this, we compare four representative indices, $p = 0.5, 1.0, 1.5,$ and 2.0 , and assess which density law best reproduces the infrared constraints. The parameter p is introduced as an effective index to account for uncertainties in the radial dis-

arXiv:2511.11835v2 [astro-ph.GA] 15 Mar 2026

tribution of the dusty material within the outflow or obscuring medium.

Beyond dynamics, AGN dust exhibits distinctive chemical compositions. Crystalline silicates, rare in the general ISM, can reach up to 20% abundance in AGN environments, possibly forming via non-equilibrium condensation in hot outflows (García-Burillo et al. 2021). Carbonaceous dust is also often enhanced, with elevated C/Si mass ratios and dust-to-gas ratios up to ten times those in the typical ISM (Shi et al. 2006; Galimore et al. 2016). These findings suggest a multi-component dust structure: silicates dominate MIR absorption, carbonaceous grains control UV obscuration, and small grains contribute to the overall infrared emission.

The observed infrared emission from a galaxy’s circumnuclear region typically has two primary contributors: thermal radiation from AGN-heated dust and light from starburst (SB). Ignoring the contribution from a SB can severely bias the interpretation of AGN spectra, as features like PAH emission lines and the cooler continuum are often misattributed to the central engine. Such contamination distorts key derived properties—including silicate feature strength, viewing angle, and extinction—while also affecting energy budgets and the classification of the system’s dominant power source (Genzel et al. 1998; Spoon et al. 2007). Consequently, it has become standard practice to explicitly model the SB component in infrared diagnostics to separate the host and nuclear emission in integrated spectra, thereby reducing systematic errors from component mixing (Laurent et al. 2000; Nardini et al. 2008).

In summary, a comprehensive model of the AGN dusty torus must simultaneously address three integrated physical components: the intrinsic dust microphysics, the disentanglement of circumnuclear star formation, and the anisotropic radiation field of the MHD wind models provide a promising dynamical framework for such structures, the resulting radial density distribution ($n(r) \propto r^{-p}$) remains a subject of active debate. Although a self-similar solution typically suggests $p \approx 1$, the complex interplay between magnetic driving, radiation pressure, and gravitational confinement may lead to a broader range of structural configurations.

The primary contribution of this work is the development of a physically motivated 3D radiative transfer framework for dusty AGN tori, where the optical depth is self-consistently computed from a parameterized MHD wind density field. We use this framework to construct an extensive library of torus spectral energy distributions (SEDs) and forward-model rest-frame MIR spectra observed with JWST/MIRI-MRS for a sample of 25 AGN. By performing a detailed Bayesian decomposition, we assess whether a universal density law can describe the circumnuclear dust or if a structural dichotomy exists among the sample. Furthermore, we quantify the systematic p -degeneracy between the radial density law and the inferred AGN fractional contribution (f_{AGN}), providing a quantitative basis for interpreting high-quality JWST MIR observations.

The paper is arranged in the following order. In Section 2 we describe the physical and computational details of our model. In Section 3 we present the results of our simulations, including the application of our models to observational data. Finally, in Section 4, we discuss the implications of our work and present our conclusions.

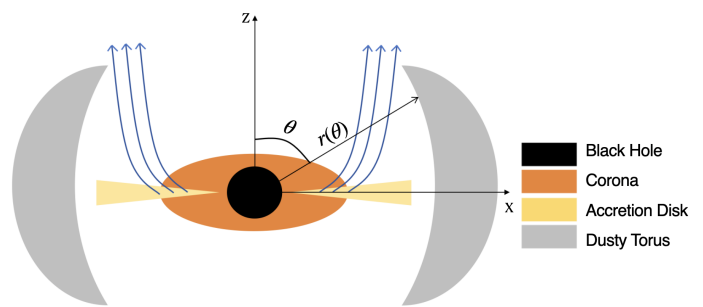


Fig. 1: Simplified 2D schematic of an AGN, illustrating key structural components including the central black hole (black), surrounding hot corona (orange), accretion disk (yellow), and obscuring dusty torus (gray). Blue lines represent the outflowing winds launched from the accretion disk, and $r(\theta)$ is the inner radius of the dusty torus with an inclination angle θ .

2. Model

2.1. AGN

We model the AGN as a central supermassive black hole (SMBH) surrounded by a geometrically thin, optically thick accretion disk and an X-ray emitting hot corona (Fig. 1). The disk emission is described by a thermal component, while the coronal continuum is represented by a power law produced by inverse-Compton scattering of disk photons (Shakura & Sunyaev 1973; Haardt & Maraschi 1993). The balance between these two components, often characterized by the optical-to-X-ray spectral index (α_{OX}), determines the overall shape of the continuum (Lusso et al. 2016). The resulting SED shape is assumed to be independent of viewing angle (Fig. 2; Sarangi et al. 2019); only the bolometric luminosity varies with inclination.

To account for anisotropic emission from a disk-like source, we scale the emitted luminosity with polar angle θ as

$$L(\theta) = \eta \dot{m} L_{\text{Edd}}(M_8) f(\theta), \quad (1)$$

where η denotes the radiative efficiency (typically ranging from 0.1 to 1), and $\dot{m} = \dot{M}/\dot{M}_{\text{Edd}}$ is the normalized accretion rate. The Eddington accretion rate is defined as $\dot{M}_{\text{Edd}} = L_{\text{Edd}}/c^2$, with L_{Edd} representing the Eddington luminosity, which scales linearly with the black hole mass M_{BH} . For convenience, the black hole mass is expressed in units of $M_8 = M_{\text{BH}}/10^8 M_{\odot}$ (Sarangi et al. 2019). The angular modulation is described by (Netzer 1987; Stalevski et al. 2012)

$$f(\theta) = \frac{1}{3} \cos \theta (1 + 2 \cos \theta). \quad (2)$$

We explore the parameter grid listed in Table 1, with $M_{\text{BH}} = 10^6 - 10^9 M_{\odot}$, $\dot{m} = 0.1 - 1$ and a fixed radiative efficiency $\eta = 0.3$. The SED shown in Fig. 2 is at $\theta = 75^\circ$, and for other inclinations we rescale the bolometric luminosity using Eqs. (1) and (2).

2.2. Dust in the dusty torus

The dusty torus in AGN is located close to the central engine and is subject to intense radiation fields. With a typical spatial extent of only a few tens of parsecs, direct observational constraints on the dust composition, size distribution, and spatial structure remain limited due to current resolution capabilities. Although recent advances in infrared interferometry and high-resolution

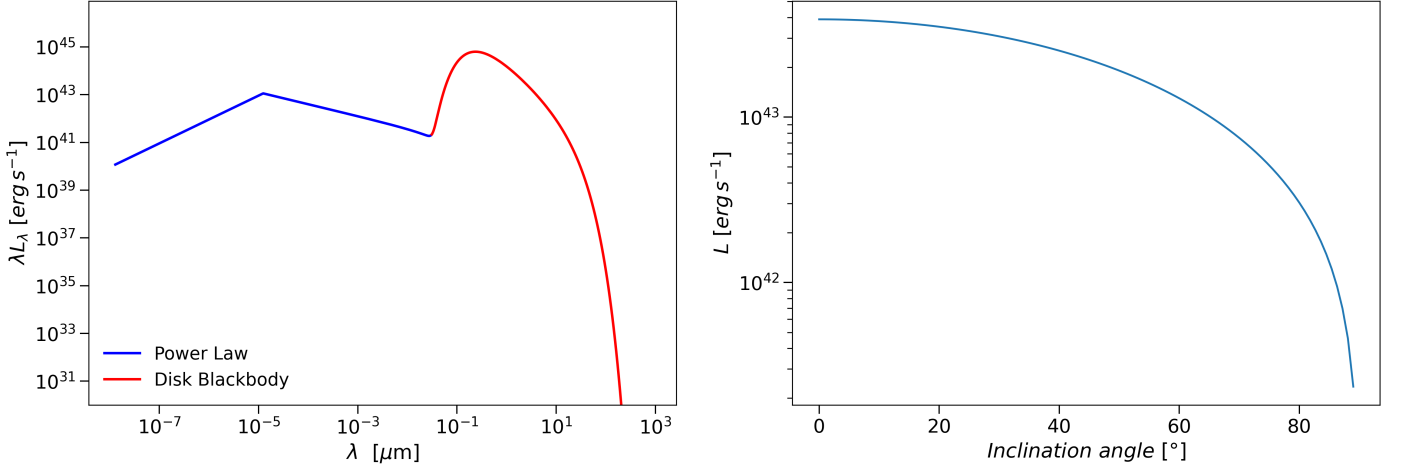


Fig. 2: Left panel: spectral energy distribution of the central AGN source at an inclination angle of $\theta = 75^\circ$. The spectral shape, characterized by $\alpha_{\text{ox}} = -1.5$, remains consistent across all viewing angles (Sarangi et al. 2019). The surrounding material is entirely heated by the central AGN radiation. right panel: angle-dependent luminosity function, following the luminosity profile defined in Eq. (2), showing how the observed emission varies with inclination angle due to anisotropic radiation effects.

imaging have improved our understanding of the torus morphology, detailed information about the physical nature of the dust grains remains elusive.

Given these observational limitations, many theoretical models have historically relied on simplified dust properties analogous to those of the diffuse ISM. These typically consist of a mixture of silicate and amorphous carbon grains, following the standard Mathis, Rumpl, and Nordsieck (MRN) power law size distribution ($n \propto a^{-3.5}$) (Mathis et al. 1977). While these simplified, ISM-like dust models do not capture the full complexity of AGN environments, they provide a robust baseline for isolating the effects of other key parameters. By establishing a physically motivated foundation that can reproduce the average AGN SED, such models are ideal for exploring the impact of torus geometry and the radiation field. Therefore, in this study, we adopt a standard ISM-based dust model to specifically investigate how changes in the torus structure and its irradiation shape the emergent infrared emission.

2.2.1. Dust properties

We adopt the AstroDust grain model of Draine & Hensley (2021) for the dusty torus. The corresponding optical properties reproduce the main MIR silicate features commonly discussed in AGN torus models (e.g. Fritz et al. 2006; Draine & Li 2007; Nenkova et al. 2008). We use the AstroDust material density $\rho_{\text{Ad}} = 2.74 \text{ g cm}^{-3}$.

For a grain size distribution discretized in bins a_i , we compute the mass-weighted absorption coefficient as

$$\kappa_{\text{abs}}(\lambda) = \sum_i w_i^m \kappa_{\text{abs}}(a_i, \lambda), \quad (3)$$

with

$$w_i^m = \frac{m(a_i) n(a_i)}{\sum_i m(a_i) n(a_i)}, \quad (4)$$

where $m(a_i)$ is the mass of a grain of size a_i and $n(a_i)$ is the corresponding number density.

Since scattering is not treated explicitly, we approximate its impact on attenuation by adopting the effective absorption coefficient

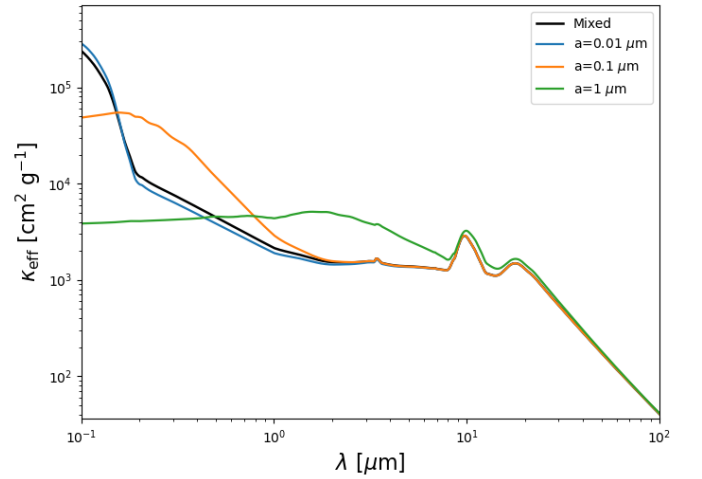


Fig. 3: Effective absorption coefficient κ_{eff} of AstroDust as a function of wavelength for different grain sizes, $0.01 \mu\text{m}$ (blue), $0.1 \mu\text{m}$ (yellow), $1 \mu\text{m}$ (green) and a mixed population (black). (Hensley & Draine 2023).

efficient (Rybicki & Lightman 1979)

$$\kappa_{\text{eff}}(\lambda) = \sqrt{\kappa_{\text{abs}}(\lambda) \kappa_{\text{ext}}(\lambda)}. \quad (5)$$

Figure 3 shows $\kappa_{\text{eff}}(\lambda)$ for selected grain sizes and for the full size distribution used in this work (Hensley & Draine 2023).

2.2.2. Dusty torus geometry

The geometry of the dusty torus is primarily governed by the physical conditions required for dust survival and by dynamical constraints imposed by the environment. The innermost boundary of the dusty structure is set by the dust sublimation radius, which corresponds to the location where the heating and cooling of dust grains are in radiative equilibrium. Dust grains can survive at this radius provided their temperature does not exceed the sublimation threshold (Dwek 1987).

The radiative heating rate of dust grains at a distance D from the central source and at an inclination angle θ is given by

$$H_d(\theta, D) = \int \bar{m} \kappa_{\text{eff}}(\lambda) \frac{L_\lambda^s(\lambda, \theta)}{4\pi D^2} d\lambda, \quad (6)$$

where \bar{m} is the average mass and $L_\lambda^s(\lambda, \theta)$ is the monochromatic luminosity of the central source as seen from angle θ . The corresponding cooling rate due to thermal re-emission is

$$L_d(T_d) = \int 4\pi \bar{m} \kappa_{\text{eff}}(\lambda) B_\lambda(\lambda, T_d) d\lambda, \quad (7)$$

where $B_\lambda(\lambda, T_d)$ is the Planck function at the dust temperature T_d . By equating the heating and cooling terms, the dust sublimation radius for a temperature of $T_d = 1500\text{K}$ can be expressed as

$$R_{1500\text{K}}(\theta) = \sqrt{\frac{\int \bar{m} \kappa_{\text{eff}}(\lambda) L_\lambda^s(\lambda, \theta) d\lambda}{4\pi L_d(1500\text{K})}}. \quad (8)$$

This defines the inner radius, R_{in} , at which dust grains can remain thermally stable without sublimating under the incident radiation field. The sublimation zone, defined by $T_{\text{dust}} \geq 1500\text{K}$, is clearly separated from the condensation zone ($T_{\text{dust}} < 1500\text{K}$) by a distinct boundary. Dust formation and survival are only permitted in the condensation zone, where thermal conditions allow for stable grain existence.

The spatial extent of the torus is set by its inner and outer radii. The outer radius is parameterized as

$$R_{\text{out}} = Y R_{\text{in}}, \quad (9)$$

where Y is a dimensionless radial extent parameter (Table 1). We assume an axisymmetric torus with a half-opening angle θ_{open} ; the polar cone ($\theta < \theta_{\text{open}}$) is taken to be dust-free.

2.2.3. Dust spatial distribution and density laws

The torus emission depends sensitively on how dust is distributed in space. In wind-driven scenarios, dust is expected to be embedded in the outflowing gas and approximately co-spatial with it over the region where grains can survive. We therefore prescribe the gas density structure and convert it to a dust density via a constant dust-to-gas mass ratio, \mathcal{D} .

We adopt a parameterized density law motivated by the self-similar MHD disk-wind solution of [Fukumura et al. \(2010\)](#). We assume axisymmetry and define the dimensionless radius $X \equiv r/R_{\text{sch}}$, where R_{sch} is the Schwarzschild radius of the central black hole. In spherical coordinates (r, θ) , the hydrogen nuclei number density is written as

$$n(r, \theta) = \mathcal{N}(p) n_0 \frac{\dot{m}}{M_8} X^{-p} \exp\left[\frac{5}{2} \left(\theta - \frac{\pi}{2}\right)\right], \quad (10)$$

where $n_0 = 5 \times 10^{10} \text{ cm}^{-3}$ is a normalization constant, $M_8 \equiv M_{\text{BH}}/(10^8 M_\odot)$. The parameter p controls the radial density gradient. We adopt $p = 1$ as a fiducial value, corresponding to the standard scaling for magnetocentrifugal disk winds ([Blandford & Payne 1982b](#); [Sarangi et al. 2019](#)). For comparison, $p = 2$ approaches the $n \propto r^{-2}$ behavior of an isotropic constant-velocity outflow ([Elvis 2000](#)). We additionally explore intermediate/shallower cases ($p = 0.5$ and $p = 1.5$) to span a broader range of gradients commonly adopted in dusty torus models (e.g., [Fritz et al. 2006](#); [Stalevski et al. 2012](#); [Everett 2005](#)).

Changing p at fixed normalization modifies not only the radial distribution but also the total column intercepted along a

given direction. To isolate the effect of the density gradient, we enforce that the radial hydrogen column density

$$N_{\text{H}}(\theta) = \int_{R_{\text{in}}}^{R_{\text{out}}} n(r, \theta) dr \quad (11)$$

is conserved at each polar angle θ relative to the fiducial $p = 1$ model. This requirement sets the p -dependent normalization factor $\mathcal{N}(p)$ to

$$\mathcal{N}(p) = \frac{(1-p) \ln(Y)}{Y^{1-p} - 1}, \quad (12)$$

so that $\mathcal{N}(p=1) = 1$. With this choice, models with different p share the same $N_{\text{H}}(\theta)$ (for fixed Y) while differing only in how that column is distributed with radius.

In the shielded dusty regions relevant for the torus, the gas mass is dominated by hydrogen; we therefore identify $n(r, \theta) \equiv n_{\text{H}}(r, \theta)$. The dust mass density is then

$$\rho_{\text{dust}}(r, \theta) = \mathcal{D} m_{\text{H}} n(r, \theta), \quad (13)$$

where m_{H} is the mass of a hydrogen atom. We explore \mathcal{D} in the range 10^{-4} – 10^{-2} , spanning from dust-poor environments to approximately solar-metallicity conditions (e.g., [Draine & Li 2007](#); [Rémy-Ruyer et al. 2014](#); [Valiante et al. 2011](#)). The full set of model parameters is summarized in Table 1.

Table 1: Model Parameters

Parameter	Adopted values
M_{BH}	$10^6, 5 \times 10^6, 10^7, 5 \times 10^7, 10^8, 5 \times 10^8, 10^9 M_\odot$
\dot{m}	0.1, 0.3, 0.5, 0.8, 1.0
$\log \mathcal{D}$	-2.0, -2.4, -2.8, -3.2, -3.6, -4.0
η	0.3
α_{OX}	-1.5
θ_{open}	$20^\circ, 30^\circ, 40^\circ, 50^\circ, 60^\circ$
θ_{view}	$0^\circ, 10^\circ, 20^\circ, 30^\circ, 40^\circ, 50^\circ, 60^\circ, 70^\circ, 80^\circ, 90^\circ$
R_{in}	$R_{1500\text{K}}$
Y	20, 60, 100, 140, 180

2.2.4. Radiative Transfer Modeling

We compute the dust temperature distribution and emergent SEDs with a deterministic 3D ray-tracing scheme on an axisymmetric dusty torus. The dust optical properties are taken from the `Astrodust` mixture (Section 2.2.1). Throughout the radiative transfer we use a wavelength-dependent effective opacity, $\kappa_{\text{eff}}(\lambda)$, evaluated with the same mass-weighted prescription as Eq. (3) but using the effective cross sections adopted in our scheme. For a dust mass column density Σ_{d} , the optical depth is

$$\tau_\lambda = \kappa_{\text{eff}}(\lambda) \Sigma_{\text{d}}. \quad (14)$$

At each location the dust temperature T_{d} is obtained by imposing local radiative equilibrium. Using the heating and cooling rates (Eqs. 6 and 7), we solve for T_{d} such that absorbed and emitted power balance.

Synthetic SEDs are computed by a formal solution along rays toward an observer at viewing angle θ_{view} . The total observed luminosity is obtained by summing the contribution of all volume elements, where each cell emits thermally and is attenuated by the optical depth accumulated from the cell to the outer boundary along the line of sight. Denoting the dust mass

Table 2: SB reference objects

Object	RA (J2000)	Dec (J2000)	z
Arp 220	15:34:57.2	+23:30:11	0.0181
M 82	09:55:52.7	+69:40:46	0.0007
Mrk 52	12:25:42.7	+00:34:20	0.0079
NGC 253	00:47:33.1	-25:17:18	0.0008
NGC 1614	04:33:59.8	-08:34:44	0.0159
NGC 7714	23:36:14.1	+02:09:19	0.0093
IRAS 17208-0014	17:23:21.9	-00:17:00	0.0428

Notes. Values compiled from commonly used NED/SIMBAD entries and rounded.

density by ρ_{dust} , the cell emissivity is taken to be proportional to $\rho_{\text{dust}} \kappa_{\text{eff}}(\lambda) B_{\lambda}(\lambda, T_d)$. The emitted luminosity can be written as

$$L_{\lambda}^{\text{obs}}(\theta_{\text{view}}) = \int_V 4\pi \rho_{\text{dust}}(r, \theta) \kappa_{\text{eff}}(\lambda) B_{\lambda}(\lambda, T_d) \times \exp[-\tau_{\lambda}(r, \theta; \theta_{\text{view}})] dV. \quad (15)$$

The computational domain is discretized on a spherical polar grid (r, θ, ϕ) with logarithmic spacing in r to resolve the strong gradients near the sublimation front. In the calculations presented here we use $N_r = 100$, $N_{\theta} = 100$, and $N_{\phi} = 20$.

As a consistency check, we verify global energy conservation by confirming that the total absorbed primary luminosity is balanced by the integrated dust infrared emission.

2.3. Starburst

Table 2 lists the J2000 coordinates and systemic redshifts (z) of the galaxies used as SB templates in this work. With the exception of Arp 220, M 82, and NGC 253, all objects are selected from the Spitzer/IRS starburst sample of Brandl et al. (2006) and are classified there as starburst-dominated systems. In our analysis, these templates provide only the SED shapes; the absolute normalization is determined during the fit to each target.

In addition, we include three well-studied systems, Arp 220, M 82, and NGC 253, as representative SB templates. Arp 220 is an ultraluminous infrared galaxy (ULIRG), $L_{\text{IR}} \gtrsim 10^{12} L_{\odot}$, from a late-stage merger with extreme dust obscuration and a very compact nuclear starburst; its MIR shows deep $9.7 \mu\text{m}$ silicate absorption and weak apparent PAH features, and its SED peaks sharply in the far-IR (Sanders & Mirabel 1996; Downes & Solomon 1998; Polletta et al. 2007). M 82 is the nearby prototypical starburst, with strong PAH emission, prominent MIR fine-structure lines, moderate silicate absorption, and a relatively warm far-IR color; we follow common empirical representations (Silva et al. 1998; Förster Schreiber et al. 2003; Polletta et al. 2007). NGC 253 is a nearby dusty nuclear starburst with strong PAH features and bright far-IR/submillimeter emission; its Spitzer/IRS spectrum places it firmly among starburst-dominated systems (Brandl et al. 2006; Radovich et al. 2001; Dale et al. 2012). Together these three templates span a useful range of obscuration, PAH strength, and dust temperature, and thus provide complementary SED shapes for our fits.

Fig. 4 compares these three representative SB templates after uniform preprocessing and normalization. All spectra have been shifted to the rest frame and resampled onto our fitting wavelength grid. For visualization, each template is normalized by its rest-frame flux density at $25 \mu\text{m}$, $F_{\text{norm}}(\lambda) = F_{\lambda}(\lambda)/F_{\lambda}(25 \mu\text{m})$, so that the curves intersect at unity at $25 \mu\text{m}$; the absolute scaling

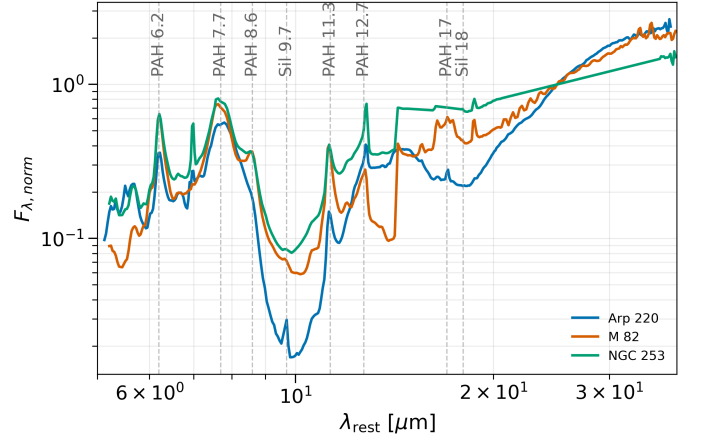


Fig. 4: Rest-frame MIR starburst templates used in this work. Normalized F_{λ} spectra of Arp 220 (blue), M 82 (orange), and NGC 253 (green) are shown as a function of λ_{rest} . Prominent PAH complexes at 6.2 , 7.7 , 8.6 , 11.3 , 12.7 , and $17 \mu\text{m}$ and the silicate absorption features at 9.7 and $18 \mu\text{m}$ are indicated by vertical dashed lines.

is free in the fits. Vertical dashed lines mark the principal PAH and silicate features.

In the following section we describe how these SB templates are combined with the AGN and BB components and fit to the JWST/MRS spectra.

2.4. Spectral decomposition and Bayesian grid inference

To constrain the physical conditions in the AGN circumnuclear region, we decompose the rest-frame $8\text{--}20 \mu\text{m}$ spectra into a linear combination of three physically motivated components: (i) an AGN torus, (ii) a host-galaxy starburst, and (iii) a warm dust continuum. The model flux is

$$\lambda F_{\lambda}^{\text{mod}} = c_{\text{AGN}} \lambda F_{\lambda}^{\text{AGN}} + c_{\text{SB}} \lambda F_{\lambda}^{\text{SB}} + c_{\text{BB}} \lambda F_{\lambda}^{\text{BB}}(T), \quad (16)$$

where $c_i \geq 0$ are non-negative scaling coefficients and $F_{\lambda}^{\text{BB}}(T)$ is a single-temperature blackbody. We scan $T = 50\text{--}350 \text{K}$, which brackets typical cold-to-warm dust temperatures while avoiding extreme values that would become degenerate with the MIR torus or starburst continua.

2.4.1. Likelihood

Before fitting, we normalize the observed JWST spectrum and all templates by their median flux over the fitted wavelength range. For each point in the discrete template grid (AGN template, SB template, and blackbody temperature T), we solve for the non-negative amplitudes (c_{AGN} , c_{SB} , c_{BB}) using non-negative least squares (NNLS), enforcing $c_i \geq 0$.

To perform the Bayesian inference, we adopt a wavelength-dependent Gaussian likelihood with an error floor,

$$\sigma_{\lambda, \text{eff}}^2 = \sigma_{\lambda, \text{stat}}^2 + (f_{\text{sys}} \lambda F_{\lambda}^{\text{obs}})^2, \quad (17)$$

where we fix $f_{\text{sys}} = 0.04$. The log-likelihood is

$$\ln \mathcal{L} = -\frac{1}{2} \sum_{\lambda} \left[\frac{(\lambda F_{\lambda}^{\text{obs}} - \lambda F_{\lambda}^{\text{mod}})^2}{\sigma_{\lambda, \text{eff}}^2} + \ln(2\pi\sigma_{\lambda, \text{eff}}^2) \right]. \quad (18)$$

2.4.2. Priors

For model comparison we score each grid point with

$$\ln P(\Theta | D) = \ln \mathcal{L}(D | \Theta) + \ln P(\Theta), \quad (19)$$

where Θ includes the discrete torus parameters, the SB template choice, and the BB temperature T . We adopt $P(\Theta) = P_{\dot{m}} P_{\theta_{\text{view}}}$. Values for M_{BH} and $\theta_{\text{view}}^{\text{target}}$ are taken from the literature when available; otherwise we use HyperLEDA¹ (flagged as ‘LEDA’ in Table A.1).

The accretion prior is based on the Eddington-ratio distribution function (ERDF) from Ananna et al. (2022), parameterized as a smooth double power law,

$$\Phi(\lambda_{\text{Edd}}) = \frac{1}{(\lambda_{\text{Edd}}/L_*)^{D_1} + (\lambda_{\text{Edd}}/L_*)^{D_2}}, \quad (20)$$

with $L_* = 10^{-1.338}$, $D_1 = 0.38$, and $D_2 = 2.64$. For each black hole mass M_{BH} we normalize the ERDF within the λ_{Edd} interval accessible to our torus grid,

$$\ln P_{\dot{m}} = \ln[\Phi(\lambda_{\text{Edd}})] - \ln\left(\int_{\lambda_{\text{min}}(M_{\text{BH}})}^{\lambda_{\text{max}}(M_{\text{BH}})} \Phi(\lambda') d\lambda'\right), \quad (21)$$

ensuring $P_{\dot{m}}$ is a proper density over the model-supported domain.

For the viewing angle we adopt a Gaussian prior,

$$\ln P_{\theta_{\text{view}}} = -\frac{(\theta_{\text{view}} - \theta_{\text{view}}^{\text{target}})^2}{2\sigma_{\text{view}}^2}, \quad (22)$$

where $\theta_{\text{view}}^{\text{target}}$ is taken from published torus constraints when available and otherwise from the host-galaxy disk inclination as a proxy (Table A.1). We adopt $\sigma_{\text{view}} = 15^\circ$ for literature-based torus constraints and a broader width for host-proxy or catalog-based inclinations.

We evaluate the Bayesian evidence by summing the unnormalized posterior weights over the discrete model grid,

$$\log \mathcal{Z} = \log \sum_k \exp(\log P(\Theta_k | D)), \quad (23)$$

where $\log P(\Theta_k | D) = \log \mathcal{L}(D | \Theta_k) + \log P(\Theta_k)$ is computed for each grid point k .

3. Results

3.1. Spatial and temperature distribution

Figure 5 shows the dust temperature field $T(r, \theta)$ for a representative model ($M_{\text{BH}} = 10^8 M_\odot$, $\dot{m} = 0.5$, $\theta_{\text{open}} = 40^\circ$, $Y = 100$, $\mathcal{D} = 10^{-2.8}$), plotted between the sublimation surface $R_{\text{in}}(\theta)$ and $R_{\text{out}}(\theta) = Y R_{\text{in}}(\theta)$.

The temperature field exhibits strong angular anisotropy, with more efficient heating at higher latitudes than near the equatorial plane. This anisotropic illumination imprints directly on the torus inner rim: the sublimation front $R_{\text{in}}(\theta)$ becomes distinctly non-spherical and assumes a concave, bowl-like shape, with larger radii toward polar directions than along the equator.

Across the model grid, geometric and opacity parameters primarily control the temperature extent and the relative weight of hot versus cool dust. Increasing Y extends the cool outer region, while larger \mathcal{D} increases attenuation and steepens the radial temperature decline. These trends are reflected in the SED variations discussed below (Fig. 6).

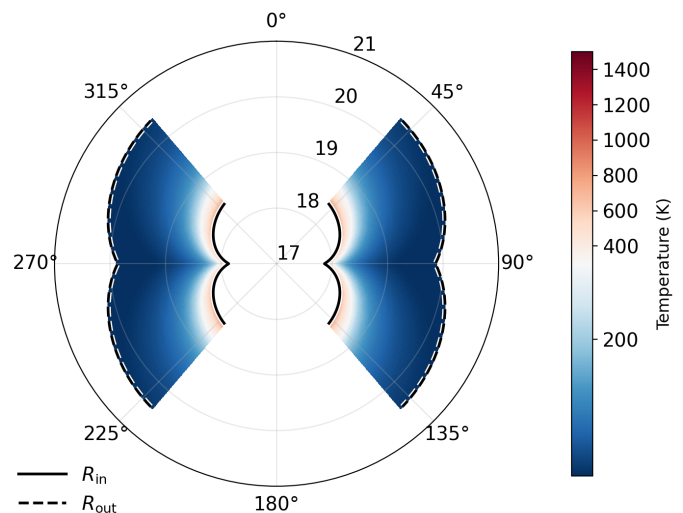


Fig. 5: Geometry–temperature polar map of the dusty torus for the representative model with $M_{\text{BH}} = 10^8 M_\odot$, $\dot{m} = 0.5$, $\theta_{\text{open}} = 40^\circ$, $Y = 100$, and $\mathcal{D} = 10^{-2.8}$. Colors indicate the dust temperature and the radial coordinate is shown as $\log_{10}(r/\text{cm})$. At each polar angle θ , the plotted domain is restricted to the dusty region between the sublimation front $R_{\text{in}}(\theta)$ (black solid curve; defined by $T_{\text{dust}} = 1500$ K) and the outer boundary $R_{\text{out}}(\theta)$ (black dashed curve), with $R_{\text{out}}(\theta) = Y R_{\text{in}}(\theta)$ by construction. The blank angular sectors correspond to the adopted polar opening cones where dust is excluded.

3.2. SED library: overview and parameter sensitivity

We build a physically motivated library of AGN SEDs over a wide parameter space. The grid spans six black hole masses, $M_{\text{BH}} \in [10^6, 10^9] M_\odot$. It also varies the normalized accretion rate \dot{m} , the dust-to-gas ratio \mathcal{D} , the torus opening angle θ_{open} , the radial extent $Y \equiv R_{\text{out}}/R_{\text{in}}$, the viewing angle θ_{view} , and the radial density index p . This library is used as the forward model in Sect. 2.4.

Figure A.1 shows the MIR behavior of the library for a representative subset. At fixed intrinsic parameters, the spectra are anisotropic. The $9.7 \mu\text{m}$ silicate feature changes with viewing angle. It can appear in emission for more face-on lines of sight and in absorption for more edge-on lines of sight. The orientation contrast becomes stronger when \mathcal{D} is higher. In that case, obscured views show deeper silicate absorption.

We then test parameter sensitivity around a fiducial model (Fig. 6). We vary one parameter at a time and keep the others fixed. Changing M_{BH} mainly shifts the overall normalization. The MIR spectral shape changes only weakly. Changing \dot{m} affects the continuum slope and the silicate feature. The trend with \dot{m} can be non-monotonic in our grid.

Parameters that set optical depth and geometry have the largest impact on the spectral morphology. Increasing \mathcal{D} strengthens silicate self-absorption. Increasing θ_{view} increases the effective line-of-sight extinction. Changing θ_{open} modifies the dust covering factor and the relative weight of hot inner emission. Increasing Y adds more cool dust at large radii. This typically reddens the MIR continuum and increases absorption.

Finally, the radial density index p is a key structural parameter. In Fig. 6, increasing p from 0.5 to 2.0 strongly suppresses the MIR output with all other parameters held fixed, and it also changes the continuum slope. Thus, MIR SEDs can be strongly

¹ <http://atlas.obs-hp.fr/hyperleda/>

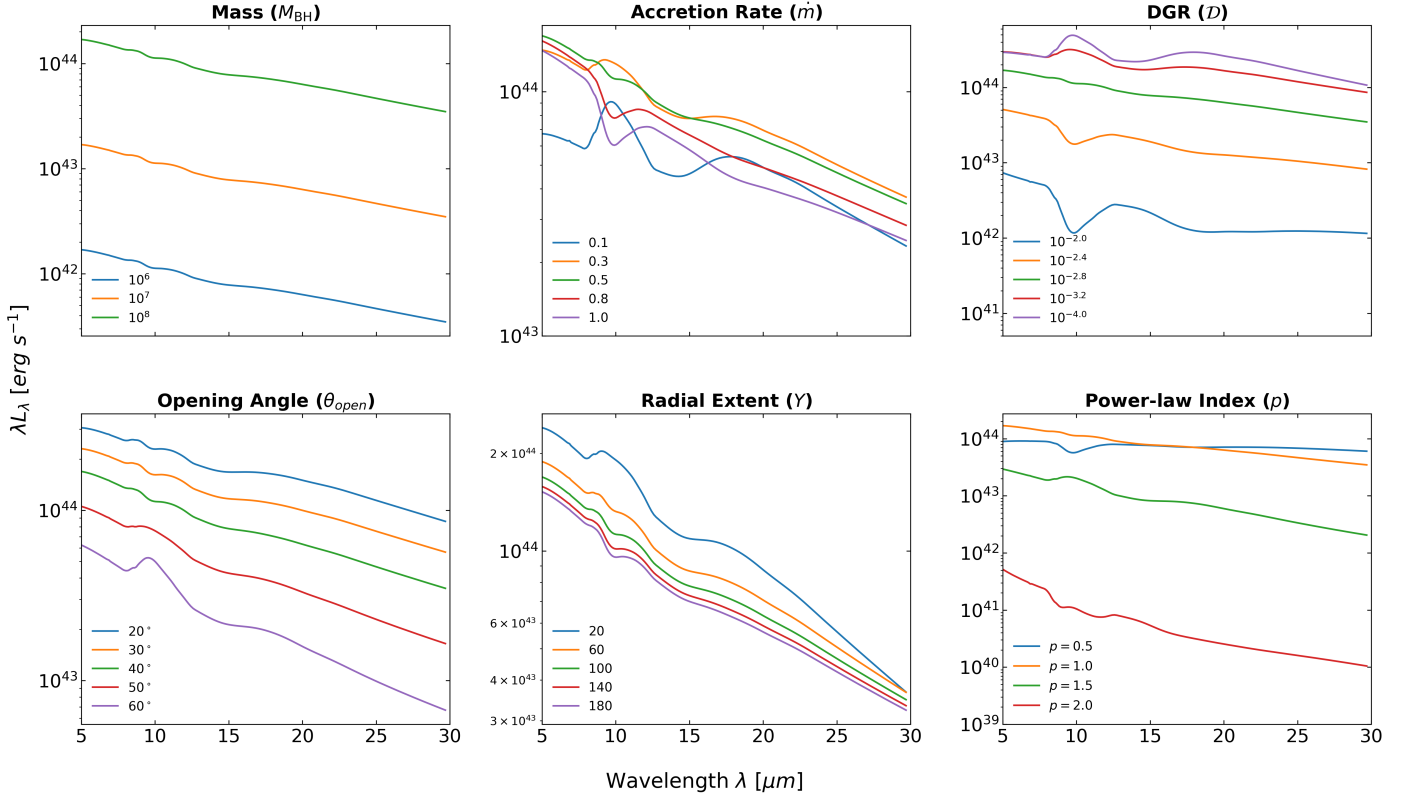


Fig. 6: One-parameter sensitivity of the infrared SED around the fiducial model (see text). Each panel varies one physical parameter while holding the others fixed, illustrating changes in both the continuum level and the $9.7 \mu\text{m}$ silicate feature.

sensitive to the assumed radial dust distribution. In the decomposition below, we therefore treat p as a structural degree of freedom and assess its impact on the inferred parameters.

3.3. Spectral decomposition results

3.3.1. Representative fits and component behavior

Figures 7 and 8 jointly illustrate the $8\text{--}20 \mu\text{m}$ spectral decomposition and the corresponding Bayesian parameter constraints for three representative sources NGC 7172, NGC 7469, and J1010+0612 (González-Martín et al. 2025; Ramos Almeida et al. 2025). Figure 7 shows that the observed spectra (black) are well reproduced by the maximum a posteriori (MAP) total model (red), expressed as the sum of three components: an AGN continuum, a SB component, and a BB continuum. The shaded regions highlight the contribution of each component to the total emission for the MAP solution and the lower panels show the residuals.

Figure 8 provides a compact, quantitative counterpart to these decompositions by showing the likelihood-weighted posterior distributions of the key parameters under different assumptions for the dust density power law index p . Several common trends emerge across the three sources. First, the inferred AGN fraction f_{AGN} broadly tracks the visual component balance in Figure 7: smoother, more weakly featured spectra favor higher f_{AGN} , whereas PAH-rich spectra favor lower f_{AGN} and a larger SB contribution. Second, the sensitivity to the assumed density profile is most pronounced for featureless spectra. In such cases, the resulting degeneracies between the torus continuum shape (governed by p) and the AGN/BB flux ratio lead to broader, shifting posteriors. Conversely, when prominent PAH complexes

are present, the star-formation component is firmly anchored, making the inferred parameters significantly less sensitive to the choice of p .

The decompositions reveal substantial diversity in the relative contributions of the inferred components. In sources with featureless, declining MIR continua, the MAP solutions prioritize the AGN component to reproduce both the absolute normalization and the spectral slope. Conversely, in spectra where PAH complexes are prominent, an enhanced SB contribution is required to fit these discrete features, consistent with PAH emission tracing star-formation-driven dust heating. The BB component is typically sub-dominant; however, for nearly featureless spectra it can trade off against the AGN continuum, contributing to the continuum-shape degeneracy discussed below.

Two limitations are apparent. For nearly featureless spectra, the AGN and BB continua are partially degenerate, which broadens the posteriors of f_{AGN} and related parameters. In addition, in several silicate-emission sources the model peak is shifted to $\sim 10.5 \mu\text{m}$, producing structured residuals; we therefore interpret parameters for these cases with caution (see Sect. 4.3).

3.4. Global parameter trends and fitting performance

Table A.2 summarizes the Bayesian evidence ($\log \mathcal{Z}$) and MAP parameters for each source across the four radial density laws. The fit quality, quantified by χ^2_{ν} , varies substantially across the sample. For most sources, we obtain $\chi^2_{\nu} \lesssim 2$ over $8\text{--}20 \mu\text{m}$; for example, NGC 1052 and MCG-05-23-016 yield $\chi^2_{\nu} \in [0.24, 1.03]$ across all p . The evidence also indicates source-dependent preferences in p : NGC 1052 and Circinus favor shallower profiles ($p = 0.5$, with $\Delta \log \mathcal{Z} > 1.8$ relative to $p = 2.0$),

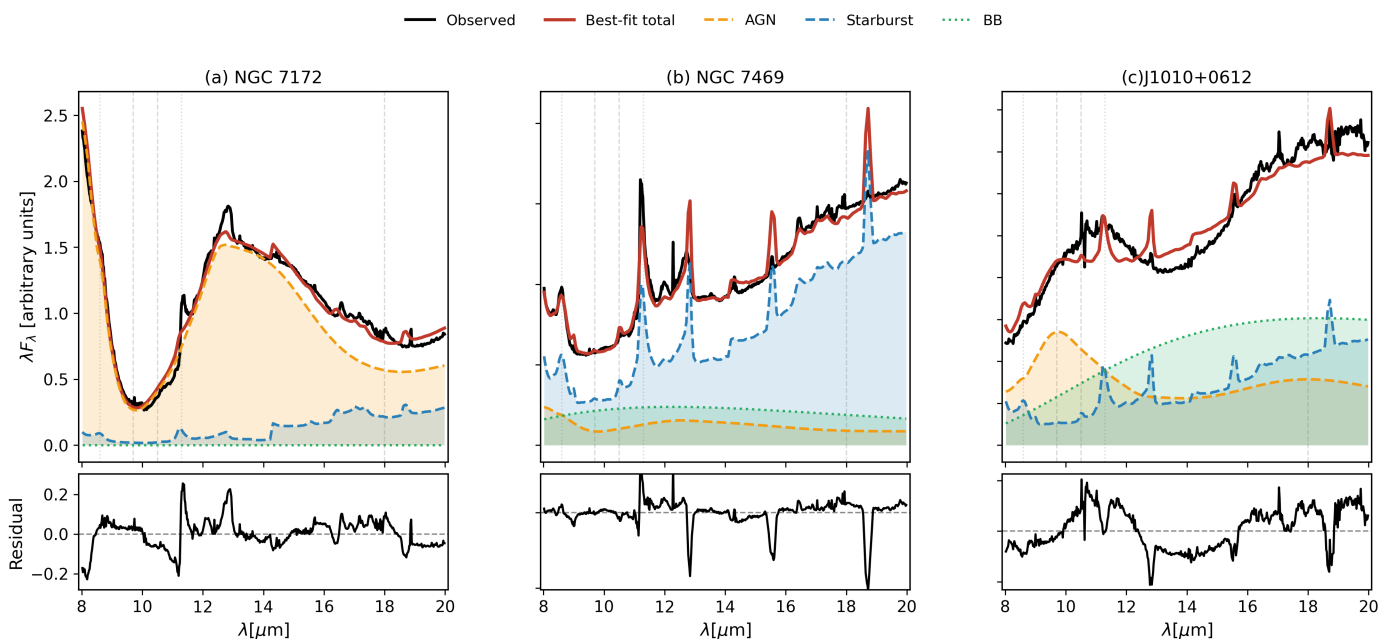


Fig. 7: MIR (8–20 μm) spectral decomposition for three sources: (a) NGC 7172, (b) NGC 7469, and (c) J1010+0612. In each panel, the black solid curve shows the observed spectrum and the red solid curve the best-fit total model. The model is decomposed into an AGN component (orange dashed), a starburst component (blue dashed), and an additional blackbody component (BB; green dotted); the shaded regions indicate the integrated contribution of each component. The lower sub-panels show the residuals, with the horizontal dashed line indicating zero residual.

whereas J1356+1026 and MRK 231 prefer steeper profiles ($p = 2.0$).

The black hole mass $\log(M_{\text{BH}}/M_\odot)$ is tightly constrained by the adopted priors based on external measurements, and it is therefore unchanged across the $p = 0.5$ – 2.0 models for most of the sample. Typical fixed values are $\log(M_{\text{BH}}/M_\odot) = 8.0$ (e.g., J1010+0612, MRK 273) and 6.6 (e.g., NGC 3081, NGC 1068). The normalized accretion rate \dot{m} is correspondingly restricted to remain consistent with the assumed mass scale and Eddington-ratio expectations: most sources converge to the lower bound $\dot{m} = 0.1$, while more moderate values ($\dot{m} \approx 0.3$ – 0.5) are found for a subset of lower-mass and/or more luminous objects (e.g., NGC 4395). With these bolometric constraints effectively fixed, changes in the radial density index p are primarily accommodated by adjustments in geometric parameters and in the BB component. For instance, in NGC 5506 the MAP value of Y increases from 100 to 180 as p steepens from 0.5 to 2.0. The blackbody temperature typically lies in the range $T \sim 200$ – 350 K, providing additional flexibility at the long-wavelength end of the MIR spectrum.

Furthermore, we find a systematic dependence of the inferred AGN fraction f_{AGN} on the radial density index p . As p increases from 0.5 to 2.0, the sample median f_{AGN} decreases from 0.403 to 0.099 (a factor of ~ 4). As shown in Table A.2, this trend holds for nearly all sources, largely independent of the silicate-feature morphology or the presence of star-formation signatures. This model-driven variation dominates the uncertainty budget of our energy decomposition. We discuss the physical origin of this p – f_{AGN} degeneracy in Sect. 4.3.

A few sources show very poor fits ($\chi_\nu^2 > 20$). For ESO 420-G13 and M 94, the large χ_ν^2 is driven by emission/absorption lines not captured by our continuum-based templates. In the starburst-dominated systems NGC 3256NUC1 and UGC 05101, a strong localized peak near 13 μm (likely [Ne II] 12.8 μm and/or

PAH 12.7 μm) biases the normalization, leaving large residuals that are insensitive to the chosen torus model.

4. Discussion and conclusions

4.1. Numerical advantages and future model extensions

The numerical framework described in Sect. 2.2.4 provides a flexible forward model for AGN MIR spectra. By solving the 3D radiative transfer problem with an anisotropic illumination pattern, the model self-consistently reproduces the angle-dependent heating that shapes the sublimation front into a bowl-like surface.

A practical advantage of our deterministic ray-tracing approach, relative to Monte Carlo radiative transfer (MCRT) codes (e.g., Stalevski et al. 2016; Stalevski et al. 2012), is that it produces noise-free model SEDs at a fixed numerical resolution, which is convenient when building large grids for Bayesian fitting. In addition, our implementation uses a logarithmic radial mesh with enhanced resolution close to the dust sublimation radius, where temperature and density gradients are steep. This combination allows efficient exploration of parameter space without stochastic fluctuations in the predicted spectra.

While the current implementation is optimized for efficient grid generation, it should be viewed as a baseline that can be extended to better capture the complexity of the circumnuclear environment. A vital future improvement is the implementation of a multi-phase dust scheme. Additionally, although the current grid is optimized for a toroidal geometry, modern high-angular-resolution observations suggest a polar-extended dust component (Hönig et al. 2012; Asmus et al. 2016). Our preference for small opening angles ($\theta_{\text{open}} \approx 20^\circ$) in several sources is consistent with a non-negligible contribution from higher-latitude dust to the MIR continuum shape. In our current static model,

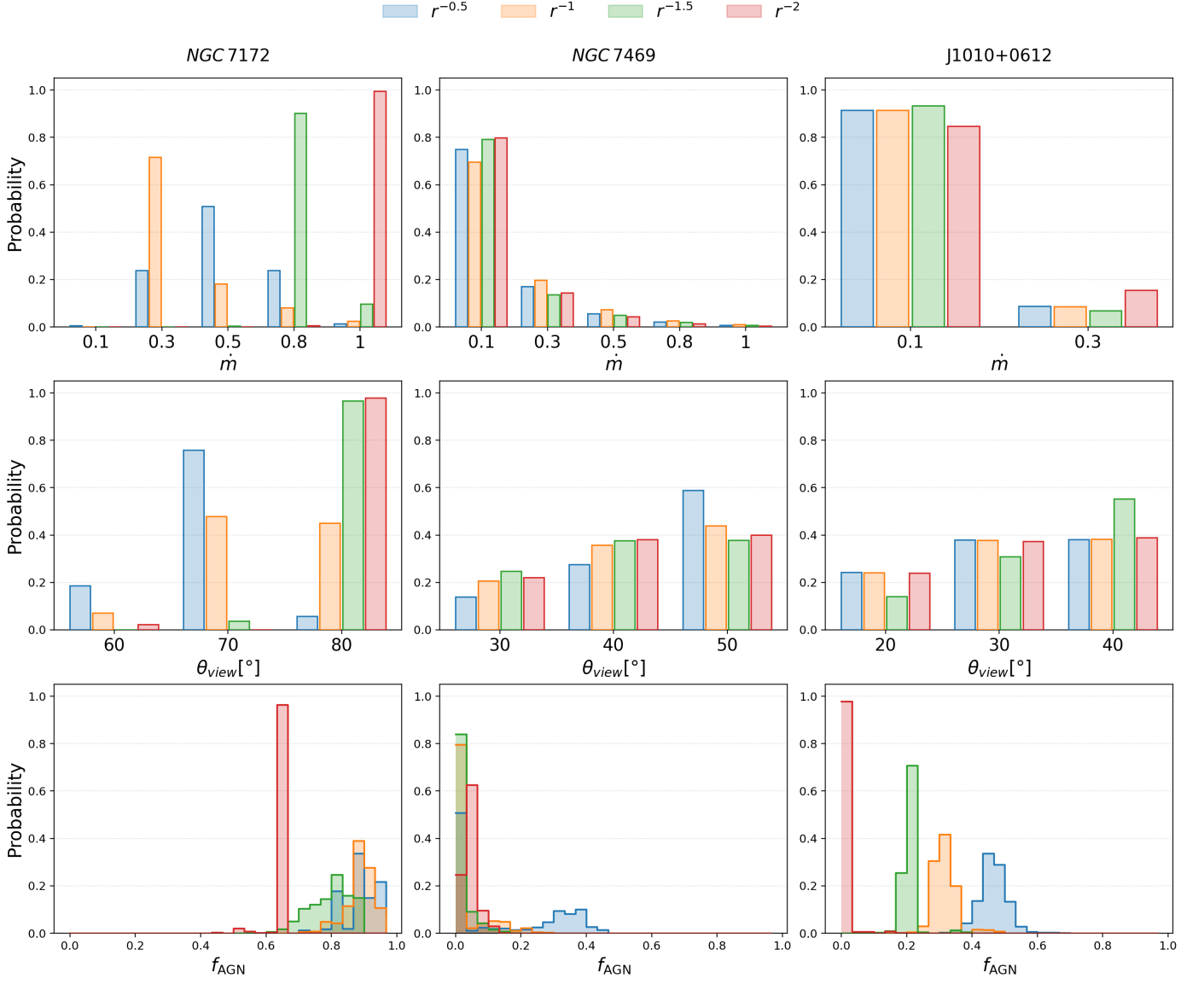


Fig. 8: Posterior probability distributions of key torus–host parameters for three representative sources (columns: NGC 7172, NGC 7469, and J1010+0612). Top row: normalized accretion rate \dot{m} . Middle row: viewing angle θ_{view} . Bottom row: AGN infrared fraction f_{AGN} . Colors show results obtained assuming different radial dust-density profiles, $n(r) \propto r^{-p}$ with $p = 0.5, 1, 1.5,$ and 2 .

this is approximated by increasing the vertical extent (opening angle θ_{open}) of the dusty torus. However, a more physically consistent approach would be to explicitly incorporate a polar wind structure, which may reduce (or remove) the need for the blackbody component. Finally, coupling this 3D dust radiative transfer with photoionization modeling would enable a simultaneous fit of both the continuum and emission-line diagnostics. Such an integrated treatment is essential to fully resolve the AGN–host interface and the complex dynamical interplay between the central engine and the circumnuclear environment.

4.2. The silicate feature: emission vs. absorption

A primary finding of this research is the contrasting behavior between silicate absorption and emission features across the sample. In obscuration-dominated sources, the silicate absorption typically appears close to $9.7 \mu\text{m}$, consistent with standard

ISM-like silicate opacity (Draine & Hensley 2021) and cold foreground dust in the torus and/or host galaxy. In contrast, in emission-dominated sources the apparent peak of the silicate emission feature is often shifted redward, with many objects peaking near $\sim 10.5 \mu\text{m}$. In the following, we discuss whether this redward shift is driven by changes in grain size and composition, radiative processing, and/or radiative transfer effects.

One plausible driver of this evolution is the intense radiation field of the central engine. High-energy photons can preferentially destroy the smallest grains or modify their size distribution, effectively suppressing the most sharply peaked contribution near the nominal $9.7 \mu\text{m}$ resonance (Laor & Draine 1993). A grain population weighted toward larger (micron-sized) grains tends to produce broader and flatter silicate profiles with enhanced red wings (González-Martín et al. 2023). In addition, the extreme thermal environment near the sublimation front can promote partial annealing of amorphous silicates into more or-

dered (crystalline) structures (Kemper et al. 2005). Although crystalline silicates primarily introduce narrow features at longer wavelengths, their presence may contribute to additional sub-structure and a relatively stronger red wing, potentially shifting the apparent emission maximum when combined with radiative transfer effects.

This redward shift can be further modulated by radiative transfer effects. Because the silicate opacity peaks near $9.7\ \mu\text{m}$, emission at this wavelength is particularly sensitive to self-absorption in media with strong temperature gradients (Nenkova et al. 2008). In such configurations, the $9.7\ \mu\text{m}$ emission emerging from the hottest surfaces can be partially absorbed by cooler dust along the line of sight, reducing the contrast at the nominal peak and moving the apparent maximum toward longer wavelengths where the optical depth is lower (Nikutta et al. 2009). This effect can help explain why absorption-dominated spectra often trace the ISM-like trough position, whereas emission-dominated spectra are more sensitive to local heating and internal obscuration.

Consequently, these results highlight the limitations of adopting fixed ISM dust templates for AGN tori. The redward shift of the emission feature is consistent with a dust population shaped by radiative processing, changes in the grain-size distribution, and internal self-absorption. Future torus models would benefit from more flexible dust prescriptions that allow the grain-size distribution and mineralogy to vary with local physical conditions, enabling a more direct connection between MIR spectral shapes and the state of the circumnuclear environment.

4.3. Fitting results and the structural p -degeneracy

Applying our 3D model library to the $8\text{--}20\ \mu\text{m}$ spectra reveals a significant p - f_{AGN} degeneracy that constitutes a major systematic uncertainty/ We find that the sample median f_{AGN} decreases four-fold as the radial density index p increases from 0.5 to 2.0.

This systematic dependence is primarily driven by the MIR continuum slope of the torus templates within our normalized fitting framework (Gandhi et al. 2009). Typical AGN spectra in the $8\text{--}20\ \mu\text{m}$ range exhibit a negative slope in λF_λ , decreasing with increasing wavelength. The radial density profile p directly dictates the steepness of this model slope. A shallow profile ($p = 0.5$) distributes a larger mass of dust to cooler, distant radii, resulting in a flatter and redder MIR continuum. To compensate for this lack of intrinsic steepness and match the observed declining slope, the fit typically compensates by increasing the f_{AGN} normalization. Conversely, a steep profile ($p = 2.0$) concentrates dust near the hot inner rim, producing a naturally steep and blue MIR continuum that intrinsically mimics the observed slope, requiring a much lower f_{AGN} weight to achieve a high-quality fit.

The Bayesian evidence ($\log \mathcal{Z}$) reveals a clear bimodal distribution in our sample: 14/25 sources favor shallow gradients ($p = 0.5$), while 8/25 prefer steep, compact configurations ($p = 2.0$), the remaining three favor intermediate gradients. This split is consistent with previous statistical studies such as García-González et al. (2017), who found that radial distributions correlate with the MIR spectral index, with Type 1 AGN tending to favor steeper distributions (warmer slopes) and Seyfert 2 galaxies favoring flatter distributions (redder slopes). Our finding of a non-universal radial structure aligns with this observed diversity across the AGN population.

This evidence split may reflect genuinely different structural states. For instance, shallow profiles ($p = 0.5$) could represent extended dust distributions influenced by MHD-driven winds,

while steep profiles ($p = 2.0$) could correspond to compact torus structures dominated by the inner rim. However, we caution that the statistical preference for these grid extremes may also serve to compensate for inherent model limitations. As discussed in Sect. 4.1, the preference for $p = 0.5$ might act as a numerical proxy for additional cool components, such as polar-extended emission, that a single power law torus cannot reproduce. Breaking this structural degeneracy will require spatial constraints from MIR interferometry (e.g., VLT/MATISSE) or high-resolution JWST imaging to definitively connect spectral shape to the true dust distribution and provide a robust energy budget for the circumnuclear environment.

4.4. Summary and Conclusions

We have developed a self-consistent 3D radiative transfer framework to model the circumnuclear dust emission in AGN dusty tori, resolving the steep temperature and density gradients near the sublimation front while ensuring bolometric energy conservation. Applying this model to a sample of 25 sources, we find that the apparent peak of the silicate emission feature is frequently shifted redward to $\sim 10.5\ \mu\text{m}$, whereas the $9.7\ \mu\text{m}$ absorption trough remains close to its canonical wavelength across the sample. This redward offset is consistent with dust in the illuminated inner regions being modified by radiative processing, potentially involving small-grain depletion, partial thermal annealing, and erosion of the resonance core by self-absorption.

Our Bayesian model comparison suggests an approximately bimodal preference in the radial density profiles ($n(r) \propto r^{-p}$): 14/25 sources favor shallow gradients ($p = 0.5$), while 8/25 prefer compact configurations ($p = 2.0$). We also identify a strong p - f_{AGN} degeneracy, with the inferred AGN fractional contribution varying by a factor of ~ 4 between shallow and steep profiles. This behavior is primarily driven by spectral-shape compensation: flatter profiles produce redder MIR continua that require a higher f_{AGN} normalization to match the data, whereas steeper profiles yield intrinsically bluer continua and thus favor lower AGN weights.

These results highlight that a major systematic uncertainty in AGN MIR energy decomposition is structural rather than purely statistical. Robust constraints on the circumnuclear dust distribution, and hence on the AGN energy budget, will require independent spatial information—for example, MIR interferometry with VLT/MATISSE and/or high-resolution JWST imaging—to break the p degeneracy and directly connect spectral curvature to the underlying geometry.

Data Availability

The simulated AGN spectra and Bayesian posterior results are available on Zenodo: <https://doi.org/10.5281/zenodo.18861234>

Acknowledgements. The authors are grateful to the anonymous referee for their constructive review and insightful suggestions, which significantly improved the clarity and depth of this paper. This work is based on observations made with the NASA/ESA/CSA James Webb Space Telescope. The data were obtained from the Mikulski Archive for Space Telescopes (MAST) at the Space Telescope Science Institute, which is operated by the Association of Universities for Research in Astronomy, Inc., under NASA contract NAS 5-03127.

References

Akylas, A., Papadakis, I., & Georgakakis, A. 2022, A&A, 666, A127

- Alonso-Herrero, A., Pereira-Santaella, M., Rieke, G. H., et al. 2013, *ApJ*, 765, 78
- Ananna, T. T., Weigel, A. K., Trakhtenbrot, B., et al. 2022, *ApJS*, 261, 9
- Antonucci, R. 1993, *ARA&A*, 31, 473
- Antonucci, R. R. J. & Miller, J. S. 1985, *ApJ*, 297, 621
- Asmus, D., Hönig, S. F., & Gandhi, P. 2016, *ApJ*, 822, 109
- Baloković, M., Cabral, S. E., Brenneman, L., & Urry, C. M. 2021, *ApJ*, 916, 90
- Behar, E. et al. 2009, *ApJ*, 703, 1347
- Beifiori, A., Sarzi, M., Corsini, E. M., et al. 2009, *ApJ*, 692, 856
- Blandford, R. D. & Payne, D. G. 1982a, *MNRAS*, 199, 883
- Blandford, R. D. & Payne, D. G. 1982b, *MNRAS*, 199, 883
- Brandl, B. R., Bernard-Salas, J., Spoon, H. W. W., et al. 2006, *ApJ*, 653, 1129
- Brenneman, L. W., Weaver, K. A., Kadler, M., et al. 2009, *ApJ*, 698, 528
- Brok, M. d., Seth, A. C., Barth, A. J., et al. 2015, *ApJ*, 809, 101
- Cruz, H. A. G., Goulding, A. D., & Greene, J. E. 2023, Modeling the SED of the AGN inside NGC 4395
- Dale, D. A., Aniano, G., Engelbracht, C. W., et al. 2012, *ApJ*, 745, 95
- Devereux, N., Ford, H., Tsvetanov, Z., & Jacoby, G. 2003, *AJ*, 125, 1226
- Downes, D. & Solomon, P. M. 1998, *ApJ*, 507, 615
- Draine, B. T. 2003, *ARA&A*, 41, 241
- Draine, B. T. & Hensley, B. S. 2021, *ApJ*, 909, 94
- Draine, B. T. & Li, A. 2007, *ApJ*, 657, 810
- Durré, M. & Mould, J. 2019, *ApJ*, 870, 37
- Dwek, E. 1987, *ApJ*, 322, 812
- Dwek, E. & Cherchneff, I. 2011, *ApJ*, 727, 63
- Elvis, M. 2000, *ApJ*, 545, 63
- Elvis, M. et al. 2002, *ApJ*, 567, L107
- Everett, J. E. 2005, *ApJ*, 631, 689
- Fernández-Ontiveros, J. A., Dasyra, K. M., Hatziminaoglou, E., et al. 2020, *A&A*, 633, A127
- Förster Schreiber, N. M., Genzel, R., Lutz, D., Sternberg, A., et al. 2003, *A&A*, 399, 833
- Fritz, J., Franceschini, A., & Hatziminaoglou, E. 2006, *MNRAS*, 366, 767
- Fukumura, K., Kazanas, D., Contopoulos, I., & Behar, E. 2010, *ApJ*, 715, 636
- Gall, C., Hjorth, J., & Andersen, A. C. 2011, *A&A Rev.*, 19, 43
- Galliano, F., Galametz, M., & Jones, A. P. 2018, *ARA&A*, 56, 673
- Gallimore, J. F. et al. 2016, *ApJ*, 829, 7
- Gandhi, P., Horst, H., Smette, A., et al. 2009, *A&A*, 502, 457
- García-González, J., Alonso-Herrero, A., Hönig, S. F., et al. 2017, *MNRAS*, 470, 2578
- García-Burillo, S. et al. 2021, *A&A*, 652, A98
- Genzel, R., Lutz, D., Sturm, E., et al. 1998, *ApJ*, 498, 579
- González-Martín, O., Díaz-González, D. J., Martínez-Paredes, M., et al. 2025, *MNRAS*, 539, 2158
- González-Martín, O., Ramos Almeida, C., Fritz, J., et al. 2023, *A&A*, 676, A73
- Haardt, F. & Maraschi, L. 1993, *ApJ*, 413, 507
- Hauser, M. G. & Dwek, E. 2001, *ARA&A*, 39, 249
- Hensley, B. S. & Draine, B. T. 2023, *ApJ*, 948, 55
- Hönig, S. F. & Kishimoto, M. 2010, *A&A*, 523, A27
- Hönig, S. F., Kishimoto, M., Antonucci, R., et al. 2012, *ApJ*, 755, 149
- Imanishi, M., Baba, S., Nakanishi, K., & Izumi, T. 2023, *ApJ*, 950, 75
- Jaffe, W. et al. 2004, *Nature*, 429, 47
- Jones, A. P. & Nuth, J. A. 2011, *A&A*, 530, A44
- Kemper, F., Vriend, W. J., & Tielens, A. G. G. M. 2005, *ApJ*, 633, 534
- Kong, M. & Ho, L. C. 2018, *ApJ*, 859, 116
- Koss, M., Trakhtenbrot, B., Ricci, C., et al. 2017, *ApJ*, 850, 74
- Laor, A. & Draine, B. T. 1993, *ApJ*, 402, 441
- Laurent, O., Mirabel, I. F., Charmandaris, V., et al. 2000, *A&A*, 359, 887
- Lopez-Rodriguez, E., Packham, C., Jones, T. J., et al. 2015, *MNRAS*, 452, 1902
- Lopez-Rodriguez, E. et al. 2020, *ApJ*, 893, 33
- Lusso, E., Worseck, G., Hennawi, J. F., et al. 2016, *MNRAS*, 456, 1253
- Marinucci, A., Bianchi, S., Nicastro, F., Matt, G., & Goulding, A. D. 2012, *ApJ*, 748, 130
- Mathis, J. S., Ruml, W., & Nordsieck, K. H. 1977, *ApJ*, 217, 425
- Narayan, R., Igumenshchev, I. V., & Abramowicz, M. A. 2000, *ApJ*, 539, 798–808
- Narayan, R. & Yi, I. 1994, *ApJ*, 428, L13
- Nardini, E., Risaliti, G., Salvati, M., et al. 2008, *MNRAS*, 385, L130
- Neenkova, M., Sirocky, M. M., Ivezić, Ž., & Elitzur, M. 2008, *ApJ*, 685, 147
- Neenkova, M., Sirocky, M. M., Nikutta, R., Ivezić, Ž., & Elitzur, M. 2008, *ApJ*, 685, 160
- Netzer, H. 1987, *MNRAS*, 225, 55
- Nguyen, D. D., Ngo, H. N., Le, T. Q. T., et al. 2025, *A&A*, 698, L9
- Nikolažuk, M., Czerny, B., & Gurynowicz, P. 2009, *MNRAS*, 394, 2141–2152
- Nikutta, R., Elitzur, M., & Lacy, M. 2009, *ApJ*, 707, 1550
- Peterson, B. M. 2014, *Space Sci. Rev.*, 183, 253
- Pier, E. A. & Krolik, J. H. 1992, *ApJ*, 401, 99
- Polletta, M., Tajer, M., Maraschi, L., et al. 2007, *ApJ*, 663, 81
- Ponti, G., Papadakis, I., Bianchi, S., et al. 2012, *A&A*, 542, A83
- Pontoppidan, K. M., Barrientes, J., Blome, C., et al. 2022, *ApJ*, 936, L14
- Radovich, M., Kahanpää, J., & Lemke, D. 2001, *A&A*, 377, 73
- Ramos Almeida, C., Asensio Ramos, A., Westerdorp Plaza, C., et al. 2025, arXiv e-prints, arXiv:2512.02629
- Roberts, C. A., Bentz, M. C., Vasiliev, E., Valluri, M., & Onken, C. A. 2021, *ApJ*, 916, 25
- Rybicki, G. B. & Lightman, A. P. 1979, Radiative processes in astrophysics
- Rémy-Ruyer, A., Madden, S. C., Galliano, F., et al. 2014, *A&A*, 563, A13
- Sanders, D. B. & Mirabel, I. F. 1996, *ARA&A*, 34, 749
- Sarangi, A., Dwek, E., & Kazanas, D. 2019, *ApJ*, 885, 126
- Shakura, N. I. & Sunyaev, R. A. 1973, *A&A*, 24, 337
- Shi, Y. et al. 2006, *ApJ*, 653, 127
- Silva, L., Granato, G. L., Bressan, A., & Danese, L. 1998, *ApJ*, 509, 103
- Spoon, H. W. W., Marshall, J. A., Houck, J. R., et al. 2007, *ApJ*, 654, L49
- Stalevski, M., Fritz, J., Baes, M., Nakos, T., & Popović, L. Č. 2012, *MNRAS*, 420, 2756–2772
- Stalevski, M., Ricci, C., Ueda, Y., et al. 2016, *MNRAS*, 458, 2288
- Tristram, K. R. W. et al. 2007, *A&A*, 474, 837
- U, V., Medling, A., Sanders, D., et al. 2013, *ApJ*, 775, 115
- Valiante, R. et al. 2011, *MNRAS*, 416, 1916
- Veilleux, S. et al. 2020, *A&A Rev.*, 28, 2
- Wada, K. 2012, *ApJ*, 758, 66
- Wada, K. et al. 2009, *ApJ*, 702, 63
- Wang, J.-M., Songsheng, Y.-Y., Li, Y.-R., Du, P., & Yu, Z. 2020, *MNRAS*, 497, 1020
- Yamada, S., Ueda, Y., Tanimoto, A., et al. 2021, *ApJS*, 257, 61
- Yan, C.-S., Lu, Y., Dai, X., & Yu, Q. 2015, *ApJ*, 809, 117
- Zhang, L., Packham, C., Hicks, E. K. S., et al. 2024, *ApJ*, 974, 195
- Zubko, V., Dwek, E., & Arendt, R. G. 2004, *ApJS*, 152, 211

Appendix A: Supplementary tables and figures

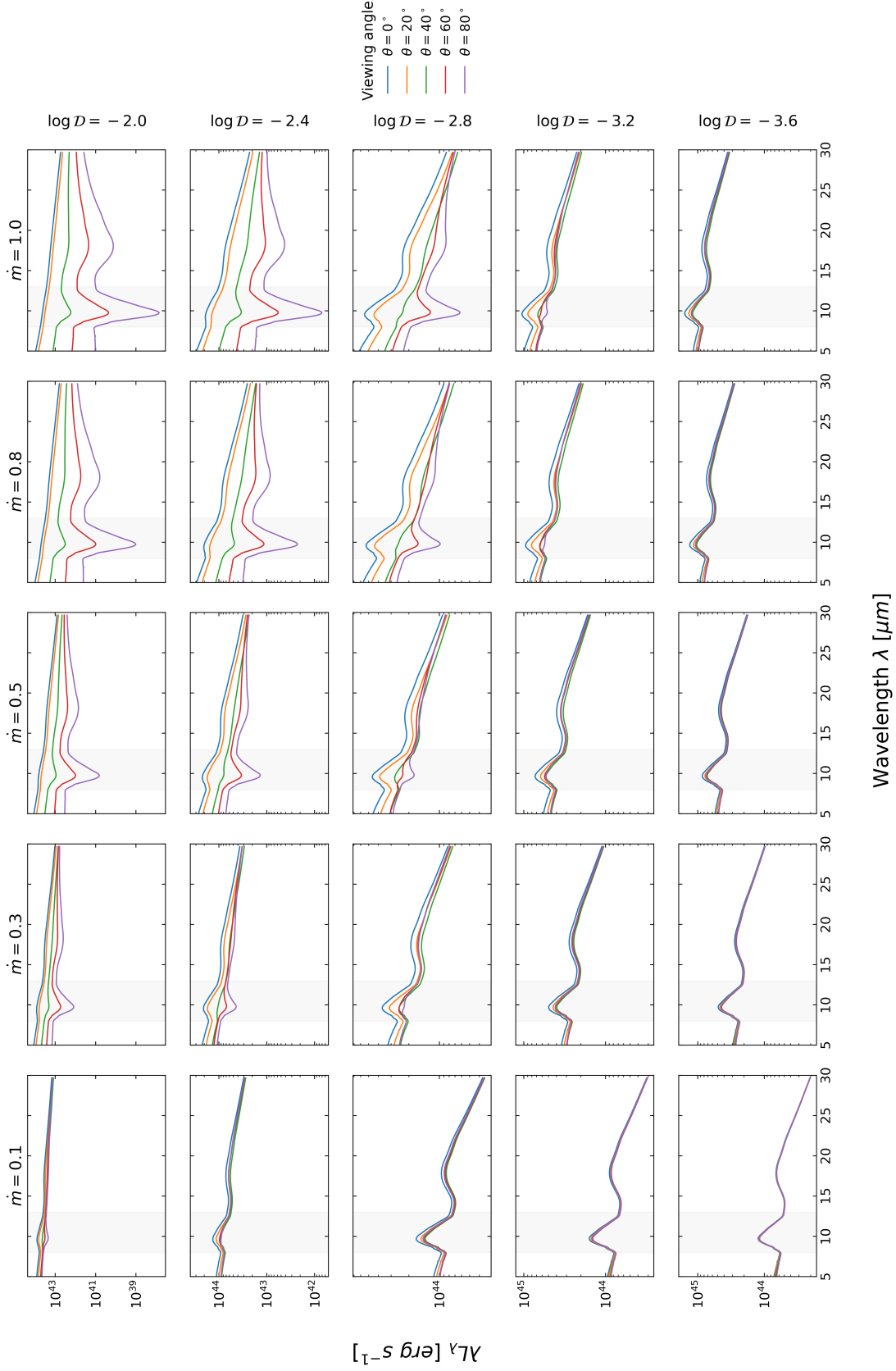


Fig. A.1: Representative grid of rest-frame infrared SEDs (λL_λ) from the torus library. Panels are organized by normalized accretion rate \dot{m} (columns) and dust-to-gas ratio \mathcal{D} (rows). Different line styles and colors indicate viewing angles $\theta_{\text{view}} \in [0^\circ, 80^\circ]$. All models adopt $M_{\text{BH}} = 10^8 M_\odot$, $Y = 100$, and $\theta_{\text{open}} = 20^\circ$. The shaded region marks the 8–13 μm silicate band.

Table A.1: JWST/MRS Extended Sample Properties

Object	RA (J2000)	Dec (J2000)	z	$E(B - V)$	M_{BH}	i_{orus}
NGC 1052	02:41:04.8	-08:15:21	0.00482	0.023	1.54×10^8 (Brenneman et al. 2009)	70 (Baloković et al. 2021)
ESO 420-G13	04:13:49.7	-30:16:28	0.01191	0.015	4×10^8 (Fernández-Ontiveros et al. 2020)	29.2 (LEDA)
UGC 05101	09:35:51.6	+61:21:11	0.03937	0.031	$1.60 \times 10^8 M_{\odot}$ (Akylas et al. 2022)	65.9 (Yamada et al. 2021)
MCG -05-23-016	09:47:40.1	-30:56:56	0.00849	0.075	$1.41 \times 10^7 M_{\odot}$ (Ponti et al. 2012)	50 (Zhang et al. 2024)
M 81	09:55:33.2	+69:03:55	0.00077	0.072	$7 \times 10^7 M_{\odot}$ (Devereux et al. 2003)	62.7 (LEDA)
NGC 3081	09:59:29.5	-22:49:35	0.00591	0.038	$8.5 \times 10^6 M_{\odot}$ - $3.4 \times 10^7 M_{\odot}$ (Beifiori et al. 2009)	71 (Zhang et al. 2024)
NGC 3256NUC1	10:27:51.3	-43:54:14	0.00935	0.120	$6.92 \times 10^6 M_{\odot}$ (Alonso-Herrero et al. 2013)	48.2 (LEDA)
NGC 4395	12:25:48.9	+33:32:48	0.00106	0.015	$1 \times 10^5 M_{\odot}$ - $1.2 \times 10^6 M_{\odot}$ (Brok et al. 2015)	10 (Cruz et al. 2023)
M 94	12:50:53.1	+41:07:14	0.00103	0.014	$1.6 \times 10^7 M_{\odot}$ (Nguyen et al. 2025)	35 (LEDA)
MRK 231	12:56:14.2	+56:52:25	0.04217	0.023	$1.5 \times 10^8 M_{\odot}$ (Yan et al. 2015)	60 (Yamada et al. 2021)
MRK 273	13:44:42.1	+55:53:13	0.03734	0.027	$1.04 \times 10^9 M_{\odot}$ (U et al. 2013)	60 (Yamada et al. 2021)
NGC 5506	14:13:14.9	-03:12:27	0.00561	0.051	$8.8 \times 10^7 M_{\odot}$ (Nikolajuk et al. 2009)	42 (Zhang et al. 2024)
NGC 5728	14:42:23.9	-17:15:11	0.00932	0.082	$3.4 \times 10^7 M_{\odot}$ (Durré & Mould 2019)	49 (Zhang et al. 2024)
IC 5063	20:52:02.3	-57:04:08	0.01135	0.055	$5.5 \times 10^7 M_{\odot}$ (Nikolajuk et al. 2009)	51 (LEDA)
NGC 7172	22:02:01.9	-31:52:11	0.00791	0.021	$5.5 \times 10^7 M_{\odot}$ (Marinucci et al. 2012)	67 (Zhang et al. 2024)
NGC 7319	22:36:03.5	+33:58:33	0.02251	0.070	$2.4 \times 10^7 M_{\odot}$ (Pontoppidan et al. 2022)	53.3 (LEDA)
NGC 7469	23:03:15.6	+08:52:26	0.01627	0.060	$1.22 \times 10^7 M_{\odot}$ (Peterson 2014)	45 (Yamada et al. 2021)
Circinus	14:13:09.9	-65:20:21	0.00145	0.463	$1.7 \times 10^6 M_{\odot}$ (Koss et al. 2017)	64.3 (LEDA)
NGC 1068	02:42:40.7	-00:00:48	0.00379	0.028	$1.3 \times 10^7 M_{\odot}$ (Wang et al. 2020)	34.7 (LEDA)
NGC 4151	12:10:32.6	+39:24:21	0.00332	0.023	$0.25 - 3 \times 10^7 M_{\odot}$ (Robertts et al. 2021)	42 (LEDA)
J1509+0434	15:09:04.2	+04:34:42	0.04410	0.041	$2.00 \times 10^8 M_{\odot}$ (Kong & Ho 2018)	44 (Ramos Almeida et al. 2025)
J1100+0846	11:00:12.4	+08:46:16	0.03120	0.025	$6.31 \times 10^7 M_{\odot}$ (Kong & Ho 2018)	38 (Ramos Almeida et al. 2025)
J1430+1339	14:30:29.9	+13:39:12	0.01700	0.031	$1.58 \times 10^8 M_{\odot}$ (Kong & Ho 2018)	38 (Ramos Almeida et al. 2025)
J1010+0612	10:10:43.3	+06:12:01	0.01430	0.022	$2.51 \times 10^8 M_{\odot}$ (Kong & Ho 2018)	35 (Ramos Almeida et al. 2025)
J1356+1026	13:56:55.7	+10:25:35	0.00700	0.019	$3.98 \times 10^8 M_{\odot}$ (Kong & Ho 2018)	55 (Ramos Almeida et al. 2025)

Notes. Astrometric and physical properties of the JWST/MIRI MRS extended sample compiled from González-Martín et al. (2025); Ramos Almeida et al. (2025). When i_{orus} is unavailable, the host disk inclination is adopted; values marked (LEDA) are taken from HyperLEDA.

Table A.2: Bayesian evidence ($\log \mathcal{Z}$) and MAP parameters for four radial density laws, $n(r) \propto r^{-p}$ with $p = \{0.5, 1.0, 1.5, 2.0\}$.

Object	p	$\log \mathcal{Z}$	χ^2_{ν}	$\log(M_{\text{BH}}/M_{\odot})$	m	θ_{view}	θ_{open}	Y	T	SB	f_{AGN}
NGC 1052	0.5	16.89	0.745	8.0	0.1	70	60	100	200	NGC7714	0.409
	1.0	16.50	0.802	8.0	0.1	70	20	100	200	NGC7714	0.288
	1.5	16.45	0.964	8.0	0.1	70	50	20	200	NGC7714	0.199
	2.0	15.07	1.025	8.0	0.1	70	20	20	200	NGC7714	0.182
ESO 420-G13	0.5	-44.83	20.044	8.0	0.1	80	60	20	100	NGC7714	0.515
	1.0	-38.72	18.223	8.0	0.1	80	60	180	100	NGC7714	0.472
	1.5	-40.90	18.305	8.0	0.3	80	60	60	300	NGC7714	0.377
	2.0	-52.31	22.062	8.0	0.3	60	60	60	250	NGC7714	0.272
UGC 05101	0.5	2.98	5.694	8.0	0.1	70	20	60	350	IRAS17208-0014	0.205
	1.0	2.80	5.798	8.0	0.1	70	40	180	200	IRAS17208-0014	0.091
	1.5	2.63	6.035	8.0	0.1	70	50	20	250	IRAS17208-0014	0.022
	2.0	2.70	5.949	8.0	0.1	70	60	100	200	IRAS17208-0014	0.048
MCG-05-23-016	0.5	18.37	0.244	6.6	0.1	50	30	180	200	M82	0.455
	1.0	17.92	0.453	6.6	0.1	60	30	180	200	NGC1614	0.267
	1.5	18.23	0.670	6.6	0.1	50	60	20	200	IRAS17208-0014	0.105
	2.0	20.88	0.281	6.6	0.1	50	60	60	200	NGC1614	0.117
M 81	0.5	1.22	5.749	8.0	0.1	60	20	100	300	NGC7714	0.452
	1.0	-0.46	6.567	8.0	0.1	60	20	60	250	NGC7714	0.375
	1.5	-4.60	7.551	8.0	0.1	70	20	140	250	NGC7714	0.316
	2.0	-10.88	9.017	8.0	0.1	70	20	140	250	NGC7714	0.235
NGC 3081	0.5	18.35	0.538	6.6	0.1	70	60	140	200	M82	0.363
	1.0	18.24	0.562	6.6	0.1	70	20	60	200	M82	0.269
	1.5	18.16	0.594	6.6	0.1	80	60	140	200	NGC1614	0.163
	2.0	18.98	0.646	6.6	0.1	70	20	180	200	NGC7714	0.099
NGC 3256NUC1	0.5	-127.55	47.008	6.6	0.5	60	40	100	50	NGC7714	0.255
	1.0	-128.61	46.962	6.6	0.8	60	20	100	50	NGC7714	0.209
	1.5	-138.56	52.841	6.6	0.1	50	20	20	150	IRAS17208-0014	0.093
	2.0	-140.69	52.529	6.6	0.3	40	60	20	200	NGC1614	0.109
NGC 4395	0.5	-16.60	10.992	6.0	0.5	20	20	140	100	NGC1614	0.530
	1.0	-18.45	11.561	6.0	0.5	10	20	180	100	NGC1614	0.388
	1.5	-24.30	13.093	6.0	0.5	20	20	20	100	NGC7714	0.298
	2.0	-35.45	15.421	6.0	1.0	20	40	180	100	NGC7714	0.228
M 94	0.5	-119.60	46.215	7.0	0.1	40	20	20	350	IRAS17208-0014	0.094
	1.0	-119.24	46.163	7.0	0.1	30	60	180	350	IRAS17208-0014	0.091
	1.5	-118.02	45.901	7.0	0.1	30	60	20	350	IRAS17208-0014	0.019
	2.0	-117.19	45.769	7.0	0.1	30	60	20	350	IRAS17208-0014	0.016
MRK 231	0.5	1.41	5.097	8.0	0.1	70	60	100	100	Arp220	0.548
	1.0	3.15	4.479	8.0	0.1	70	60	180	150	Arp220	0.405
	1.5	3.01	3.993	8.0	0.3	70	60	100	150	Arp220	0.324
	2.0	6.16	4.320	8.0	0.1	60	60	180	200	Arp220	0.179
MRK 273	0.5	8.53	1.758	8.0	0.3	70	20	180	150	IRAS17208-0014	0.290
	1.0	2.44	4.196	8.0	0.3	70	20	180	200	Arp220	0.265
	1.5	-7.09	7.479	8.0	0.3	70	40	60	200	Arp220	0.148
	2.0	-3.83	7.023	8.0	0.1	50	60	20	200	Arp220	0.111
NGC 5506	0.5	14.08	0.673	8.0	0.3	40	20	100	200	NGC1614	0.593
	1.0	12.30	0.904	8.0	0.3	50	20	180	150	IRAS17208-0014	0.559
	1.5	8.55	1.749	7.6	0.8	50	20	180	200	IRAS17208-0014	0.213
	2.0	14.30	1.484	7.6	0.1	40	60	60	200	NGC1614	0.212
NGC 5728	0.5	-66.82	29.187	7.0	0.1	50	20	60	250	IRAS17208-0014	0.086
	1.0	-66.66	29.180	7.0	0.1	60	20	180	250	IRAS17208-0014	0.037
	1.5	-66.67	29.287	7.0	0.1	50	20	100	300	IRAS17208-0014	0.000
	2.0	-66.64	29.287	7.0	0.1	50	20	100	300	IRAS17208-0014	0.000
IC 5063	0.5	17.71	0.311	7.0	0.1	50	20	180	200	NGC1614	0.403

Continued on next page

Object	p	$\log \mathcal{Z}$	χ^2_ν	$\log(M_{\text{BH}}/M_\odot)$	\dot{m}	θ_{view}	θ_{open}	Y	T	SB	f_{AGN}
	1.0	16.99	0.725	7.0	0.1	60	30	180	200	NGC1614	0.211
	1.5	16.99	1.086	7.0	0.1	50	60	180	200	IRAS17208-0014	0.080
	2.0	19.54	0.483	7.0	0.1	50	60	180	200	NGC1614	0.094
NGC 7172	0.5	0.29	4.092	7.0	0.8	70	60	100	350	M82	0.828
	1.0	4.61	3.770	7.0	0.3	80	60	20	50	M82	0.875
	1.5	0.89	3.856	7.0	0.8	80	30	20	350	M82	0.816
	2.0	-15.77	8.640	7.0	1.0	80	50	20	200	Arp220	0.647
NGC 7319	0.5	14.80	0.974	7.0	0.1	60	20	100	200	NGC1614	0.446
	1.0	12.69	1.118	7.0	0.3	50	20	180	200	NGC1614	0.241
	1.5	11.78	1.378	7.0	0.5	60	20	60	200	NGC1614	0.183
	2.0	14.69	1.508	7.0	0.1	50	60	100	200	NGC1614	0.110
NGC 7469	0.5	10.12	2.644	7.0	0.1	50	20	180	350	NGC7714	0.296
	1.0	9.71	2.554	7.0	0.3	50	20	180	300	NGC7714	0.111
	1.5	9.77	3.401	7.0	0.1	40	60	20	300	NGC7714	0.021
	2.0	11.61	2.554	7.0	0.1	40	60	180	300	NGC7714	0.037
Circinus	0.5	15.06	0.559	6.0	0.5	70	20	180	200	NGC1614	0.389
	1.0	11.42	1.763	6.0	0.5	70	20	100	200	Arp220	0.199
	1.5	5.52	2.729	6.0	1.0	70	20	20	200	Arp220	0.149
	2.0	4.98	3.909	6.0	0.5	60	60	60	200	Arp220	0.081
NGC 1068	0.5	15.29	0.963	6.6	0.1	40	20	180	200	IRAS17208-0014	0.481
	1.0	15.11	0.805	6.6	0.3	40	20	100	200	Mrk52	0.299
	1.5	16.09	1.459	6.6	0.1	30	60	20	250	NGC1614	0.042
	2.0	18.38	0.901	6.6	0.1	30	60	180	250	Mrk52	0.057
NGC 4151	0.5	18.43	0.358	6.6	0.1	50	30	20	200	M82	0.506
	1.0	18.71	0.357	6.6	0.1	50	30	60	200	M82	0.433
	1.5	19.74	0.433	6.6	0.1	40	60	20	200	M82	0.307
	2.0	18.12	0.864	6.6	0.1	40	20	20	250	Mrk52	0.110
J1430+1339	0.5	11.78	1.813	8.0	0.1	50	20	140	200	M82	0.385
	1.0	11.63	2.289	8.0	0.1	50	20	180	200	NGC1614	0.178
	1.5	11.80	2.518	8.0	0.1	40	60	20	250	NGC1614	0.012
	2.0	13.18	2.101	8.0	0.1	40	60	60	200	NGC7714	0.075
J1509+0434	0.5	10.21	2.278	8.0	0.1	50	20	180	250	NGC7714	0.207
	1.0	10.17	2.634	8.0	0.1	50	20	180	250	NGC7714	0.074
	1.5	10.46	2.718	8.0	0.1	40	60	20	250	NGC7714	0.027
	2.0	11.71	2.241	8.0	0.1	40	60	20	250	NGC7714	0.033
J1100+0846	0.5	17.51	0.807	8.0	0.1	40	20	100	250	M82	0.337
	1.0	17.59	0.894	8.0	0.1	40	20	180	250	M82	0.200
	1.5	17.74	0.971	7.6	0.1	40	20	20	200	M82	0.292
	2.0	14.67	1.859	8.0	0.1	40	20	20	250	M82	0.057
J1010+0612	0.5	9.96	2.371	8.0	0.1	40	20	180	200	NGC7714	0.459
	1.0	5.61	4.027	8.0	0.1	40	20	180	200	NGC7714	0.297
	1.5	-3.23	6.590	8.0	0.1	40	20	180	200	Mrk52	0.231
	2.0	-15.49	11.445	8.0	0.1	40	60	180	300	Mrk52	0.000
J1356+1026	0.5	14.16	1.556	8.0	0.1	60	40	60	150	Arp220	0.188
	1.0	14.36	1.507	8.0	0.1	60	40	180	150	Arp220	0.142
	1.5	14.71	1.355	8.0	0.1	50	60	20	150	IRAS17208-0014	0.050
	2.0	16.80	0.834	8.0	0.1	50	60	60	150	IRAS17208-0014	0.093